



## Synergistic effect of bimetallic Au-Ru/TiO<sub>2</sub> catalysts for complete oxidation of methanol

Lina A. Calzada<sup>a</sup>, Sebastian E. Collins<sup>b</sup>, Chang W. Han<sup>c</sup>, Volkan Ortalan<sup>c</sup>, Rodolfo Zanella<sup>a,\*</sup>

<sup>a</sup> Centro de Ciencias Aplicadas y Desarrollo Tecnológico, Universidad Nacional Autónoma de México, Circuito Exterior S/N, Ciudad Universitaria, C.P. 04510 Mexico City, Mexico

<sup>b</sup> Instituto de Desarrollo Tecnológico para la Industria Química (INTEC) – Universidad Nacional del Litoral and CONICET, Güemes 3450, C.P. 3000 Santa Fe, Argentina

<sup>c</sup> School of Materials Engineering, Purdue University, West Lafayette, IN, USA



### ARTICLE INFO

#### Article history:

Received 12 October 2016

Received in revised form 11 January 2017

Accepted 28 January 2017

Available online 8 February 2017

#### Keywords:

Methanol oxidation

Gold catalysts

Bimetallic

Ruthenium

Deposition-Precipitation

### ABSTRACT

Bimetallic Ru-Au/TiO<sub>2</sub> catalysts prepared by deposition-precipitation with urea method were tested for the first time in the total oxidation of methanol. Different Ru:Au atomic ratios were used (1:1–0.25:1). The catalytic activity results showed a synergistic effect at low temperature (RT–50 °C), mainly for the 1:1 and 0.75:1 atomic ratio. HAADF-STEM and STEM-EDS characterization confirmed the interaction between Ru and Au. TPR, UV-vis spectra, XPS and DRIFTS-CO results also confirm this interaction. FTIR spectra, recorded following the oxidation of methanol as a function of the reaction temperature, showed that formates are the main reaction intermediates in the oxidation of methanol, which are formed from RT on bimetallic Ru-Au catalysts and are oxidized at lower temperatures compared to their monometallic Ru and Au counterparts.

© 2017 Elsevier B.V. All rights reserved.

### 1. Introduction

Volatile organic compounds (VOCs), which are characterized by high vapor pressure and low water solubility, are precursors of ozone and photochemical smog. They are emitted from outdoor sources, such as transport and industrial processes as well as from indoor sources, such as household products. The most efficient and low-cost method for their abatement is the catalytic combustion to CO<sub>2</sub> and H<sub>2</sub>O, preferentially at low temperatures [1,2].

Methanol is frequently employed as a model molecule for the total oxidation of VOCs; it has been investigated using gold catalysts supported on metal oxides because gold is known to be catalytically active in oxidation reactions when it is well dispersed on reducible metal oxides. The most remarkable reaction is CO oxidation at temperatures lower than ambient [3–6], although it has also been studied in VOCs oxidation using different molecules probes as propene, benzene, hexane, ethanol, toluene and acetone [7–11]. Particularly, gold catalysts supported on metal oxides such as Fe<sub>2</sub>O<sub>3</sub> [12,13], CeO<sub>2</sub> [14,15], MCM-41 (modified by V and Nb)

[16], ZnO [17] and TiO<sub>2</sub> [18] have been investigated for the oxidation of methanol. Au/Fe<sub>2</sub>O<sub>3</sub> has shown higher catalytic activity and, in some cases, better performance than Pt and Pd catalysts for this reaction [12,13].

A few studies have been focused on explaining the reaction mechanism of the total oxidation [15,17] and decomposition of methanol [19,20] on Au supported catalysts, indicating that methoxy and formate species are the principal reaction intermediates. The reaction between methanol and surface OH groups producing methoxy species adsorbed on the support with elimination of water is generally agreed. This methoxy species are then transformed into formates and also oxidized totally to CO<sub>2</sub>. The last step is the oxidation of formates to CO<sub>2</sub>, although it has been reported that formates can also act as a catalyst poison [17]. The activation of oxygen has been proposed to be performed in the periphery of the Au particle with the support [19,20], and sometimes the support can deliver some oxygen from the lattice, as in the case of TiO<sub>2</sub>, CeO<sub>2</sub> and Fe<sub>2</sub>O<sub>3</sub> [12,14]. Scirè et al. [12,14] proposed that highly dispersed small gold particles are able to weaken the Ce–O and Fe–O bonds adjacent to the Au atom, increasing like this the mobility of the lattice oxygen, also called metal-assisted Mars–Van Krevelen mechanism.

\* Corresponding author.

E-mail address: [rodolfo.zanella@ccadet.unam.mx](mailto:rodolfo.zanella@ccadet.unam.mx) (R. Zanella).

Bimetallic catalyst systems have been employed to improve the activity, selectivity and stability, compared to their monometallic counterparts. It is known that the physical and chemical properties of bimetallic particles are different from those of the monometallic ones, including changes in their optical and electronic properties, which are tunable with composition and particle size. The final composition of these catalysts depends strongly on the method of synthesis, interaction between metals, atmosphere and temperature of activation, among others. The addition of the second component may induce significant changes in activity and selectivity, attributing the enhancement of the catalytic properties to ensemble or ligand effects [21].

It has been reported that, despite their immiscibility in bulk state [22,23], Au and Ru can interact in supported catalysts, showing an enhancement of their catalytic properties in the oxidation of methanol [24,25], glycerol [23] and CO in a mixture of CO/NH<sub>3</sub>/O<sub>2</sub> [26], compared to their monometallic counterparts. Particularly, the bimetallic Au-Ru/Fe<sub>2</sub>O<sub>3</sub> catalyst [24] exhibited a higher hydrogen production in the partial oxidation of methanol, compared to the monometallic Ru and Au catalysts. The increase in activity was attributed to the strong metal–metal and metal–support interaction in the catalyst. Sreethawong et al. [25] studied Au-Ru catalysts supported on Al<sub>2</sub>O<sub>3</sub> and SiO<sub>2</sub> observing that the interactions between Au and Ru was beneficial for the total oxidation of methanol because of the creation of different types of adsorption/desorption sites that modify the mechanism of methanol decomposition.

The aims of this work were to evaluate, for the first time, the effect of ruthenium in bimetallic Ru-Au catalysts supported on TiO<sub>2</sub> in the total oxidation of methanol as a function of the Ru:Au atomic ratio and to try to elucidate the nature of the interaction between gold and ruthenium. To obtain information about the reaction mechanism, FTIR spectra were recorded following the oxidation of methanol as a function of the reaction temperature.

## 2. Experimental

### 2.1. Preparation of catalysts

#### 2.1.1. Preparation of monometallic samples

Titania Degussa P25 was used as support (45 m<sup>2</sup> g<sup>-1</sup>, non-porous, 70% anatase and 30% rutile, purity >99.5%). Commercial HAuCl<sub>4</sub>·3H<sub>2</sub>O (Sigma) and RuCl<sub>3</sub>·3H<sub>2</sub>O (Pressure Chemical) were employed as gold and ruthenium precursors. Prior to preparation, TiO<sub>2</sub> was dried in air at 100 °C for at least 24 h. The nominal metal loadings in the monometallic catalysts were 3 wt.% for gold and 1.56 wt.% for Ru, which is equivalent to 0.4 at.% for each sample.

The preparation of the Au/TiO<sub>2</sub> sample was performed by deposition-precipitation with urea (DPU) in the absence of light, according to the previously reported procedure [27,28]. In this preparation, the HAuCl<sub>4</sub> (4.2 × 10<sup>-3</sup> M) and urea (0.42 M) were dissolved in 37 mL of distilled water. Then, 1 g of titania was added to this solution. The suspension was heated at 80 °C and kept constant for 16 h under vigorous stirring. Afterwards, the suspension was centrifuged, washed with water and centrifuged again four times. The solid recovered was dried under vacuum for 2 h at 80 °C. The monometallic Ru/TiO<sub>2</sub> sample was prepared following the same method, 1 g of titania was added to an aqueous solution (37 mL) containing RuCl<sub>3</sub> (4.2 × 10<sup>-3</sup> M) and urea (0.42 M). The suspension was stirred vigorously and kept at 80 °C for 2 h, then it was centrifuged and washed four times with water, as in the case of the Au/TiO<sub>2</sub> sample. The solid recovered in both samples was dried under vacuum for 2 h at 80 °C and stored at room temperature in a desiccator under vacuum, away from light in order to prevent any alteration [29].

#### 2.1.2. Preparation of bimetallic samples

In bimetallic samples, the nominal gold loading was kept constant (3 wt.%), whereas for ruthenium was chosen to synthesize Ru-Au catalysts with different Ru:Au atomic ratios: 1:1, 0.75:1, 0.5:1 and 0.25:1. A sequential deposition method was used to prepare these catalysts. Gold was first deposited on TiO<sub>2</sub>, according to the DPU method described above. After being dried at 80 °C for 2 h, ruthenium was also deposited by DPU as previously described. The same procedure of washing and drying as above was employed. The samples were identified as Ru-Au followed by the nominal Ru:Au atomic ratio, e.g., Ru-Au 0.75-1.

### 2.2. Characterization techniques

The elemental analysis of Au and Ru in the dried samples was performed by X-ray fluorescence (XRF) using a XEPOS HE (AMETEK) spectrometer. The Au and Ru weight loadings were expressed in grams of each metal per gram of sample.

After *ex situ* thermal treatment under the same conditions as those used for the oxidation reaction of methanol, the samples were examined by transmission electron microscopy in a Jeol-2010 FasTem analytical microscope equipped with a high-angle annular dark-field (HAADF) detector. The average size of particles and the histograms of particle sizes were obtained from the measurement of 300–500 particles. The size limit for the detection of the metal particles on TiO<sub>2</sub> was about 0.6 nm. The average particle diameter  $d_s$  was calculated with the formula:  $\sum n_i d_i / \sum n_i$ , where  $n_i$  is the number of particles of diameter  $d_i$ . The standard deviation was calculated with the formula:  $[\sum (d_i - d_s)^2 / \sum n_i]^{1/2}$ . High resolution Z-contrast scanning transmission electron microscopy (STEM) imaging and STEM energy dispersive X-ray spectroscopy (EDS) analysis were performed using a probe aberration-corrected JEOL ARM200CF equipped with an Oxford X-Max100TLE windowless detector. The microscope was operated at 200 kV. The probe current and convergent semiangle were 79 pA and 15 mrad, respectively. The collection angle of the HAADF detector was 68–280 mrad. The STEM-EDS maps, linescan profiles and compositions were collected using the Oxford Aztec software. The quantification of the compositions of bimetallic nanoparticles was performed by the Cliff-Lorimer method [30] using the Aztec software.

Diffuse reflectance UV-vis spectra of the catalysts were obtained using a CARY 5000 spectrophotometer equipped with a Praying Mantis and a high temperature reaction chamber (Harrick). The spectra were recorded from 300 to 800 nm during the activation thermal treatment under hydrogen. In each experiment, approximately 30 mg of dried sample was packed in the sample holder and pretreated *in situ* under hydrogen flow (30 mL min<sup>-1</sup> and 5 °C min<sup>-1</sup>) up to 300 °C, followed by a 60-min plateau. A spectrum of Teflon (from Aldrich) was used as reference.

The hydrogen temperature programmed reduction (H<sub>2</sub>-TPR) analysis of the dried catalysts was performed in a RIG-150 unit under a flow of 10% H<sub>2</sub>/Ar mixture (50 mL min<sup>-1</sup>) employing a heating rate of 10 °C min<sup>-1</sup> from room temperature to 600 °C. H<sub>2</sub>O produced during the reduction process was trapped before the TCD detector.

CO adsorption was followed by DRIFT spectroscopy to characterize the metallic surface. The experiments were carried out in a Nicolet 670FT-IR spectrophotometer equipped with a Praying Mantis and a low/high temperature reaction chamber (Harrick). In each experiment, approximately 40 mg of dried sample was packed in the sample holder and pretreated *in situ* under hydrogen flow (40 mL min<sup>-1</sup>, heating rate 5 °C min<sup>-1</sup>) up to 300 °C followed by a plateau of 1 h. After thermal treatment, the sample was cooled down to room temperature under the same gas flow and then purged with N<sub>2</sub> before the introduction of 5% CO in N<sub>2</sub> (40 mL min<sup>-1</sup>). A spectrum recorded under N<sub>2</sub> was used as refer-

ence, then several spectra were recorded under the CO flow until the band intensity was stable.

X-ray photoelectron spectroscopy (XPS) analyses were performed on a multi-technique (SPECS) equipment with a dual X-ray Mg/Al source and a PHOIBOS 150 hemispheric analyzer. The spectra were obtained using pass energy of 30 eV, and the Al-K $\alpha$  X-ray source was operated at 100 W. The working pressure in the analyzing chamber was less than  $2 \times 10^{-8}$  mbar. XPS spectra were acquired after an *in situ* pre-treatment under hydrogen flow at 300 °C. The binding energy (BE) scale was referenced to the peak at 289.5 eV of adventitious carbon because it is not overlapped as the usually used peak at 284.6 eV. The fitting analysis was performed using CASA XPS software.

### 2.3. Catalytic activity

The performance of the oxidation of methanol was evaluated using a continuous plug-flow microreactor at atmospheric pressure. For each experiment, 50 mg of powder catalyst diluted with 100 mg of quartz (40/60 mesh) was placed in the microreactor. The catalyst sample was first activated *in situ* under hydrogen flow (50 mL min $^{-1}$ ) with a heating rate of 5 °C min $^{-1}$  up to 300 °C, followed by a temperature plateau of 2 h. After this treatment, the sample was cooled to RT under the same gas. The reactant gas mixture (2700 ppm methanol and 20 vol.% O<sub>2</sub> balanced with He) was introduced with a total flow rate of 100 mL min $^{-1}$ , and a heating rate of 5 °C min $^{-1}$ . To keep the desired concentration of methanol, a saturator with a thermostatic bath at 5 °C was employed connected with a He flow (3.5 mL min $^{-1}$ ). All the lines in contact with methanol were warmed to prevent condensation. The outlet gas stream was analyzed continuously with a mass spectrometer (Balzers QMG 421). The following species were scanned: CH<sub>3</sub>OH ( $m/e = 31$ ), formaldehyde ( $m/e = 30$ ), CO ( $m/e = 28$ ), CO<sub>2</sub> ( $m/e = 44$ ), H<sub>2</sub>O ( $m/e = 18$ ) and H<sub>2</sub> ( $m/e = 2$ ).

To determine the reaction rates, a lower amount of catalyst was required in order to guarantee a kinetic regime (conversion <20%). For that purpose, 25 mg of catalyst was diluted in 100 mg of quartz (40/60 mesh), placed in the microreactor and tested as previously described. The turnover frequencies (TOF), number of molecules of methanol converted per surface atom of gold particles, and per second, were determined from the reaction rates (calculated at low conversion) and the dispersion of the metal (number of surface atoms/total number of atoms in the particle). The dispersion of metal was calculated with the assumption that metal particles were cuboctahedral with an hexagonal face in contact with the titania surface.

### 2.4. Temperature programmed oxidation of adsorbed methanol by transmission FTIR

The adsorption of methanol and the temperature programmed reaction with oxygen of the adsorbed species were followed by *in situ* infrared Fourier transform spectroscopy (FTIR). Self-supporting wafers of each material (25 mg, d = 13 mm, P = 5 t cm $^{-2}$ ) were placed into a Pyrex IR cell fitted with water-cooled NaCl windows, which was attached to a conventional high vacuum system, equipped with a manifold for gas flow operation. Before the adsorption of methanol, each sample was pretreated *in situ* under hydrogen flow (50 mL min $^{-1}$ , heating rate 5 °C min $^{-1}$ ) up to 300 °C followed by a plateau of 2 h. After thermal treatment, the sample was cooled down to room temperature under the same gas flow and then evacuated at room temperature. Reference IR spectra of the clean surface sample after reduction were taken at room temperature. Next, pulses of methanol (Carlo Erba RPE, 99.9%) were injected into the cell until saturation of the surface was obtained, as indicated by the steady state of the IR signals. Afterward, the

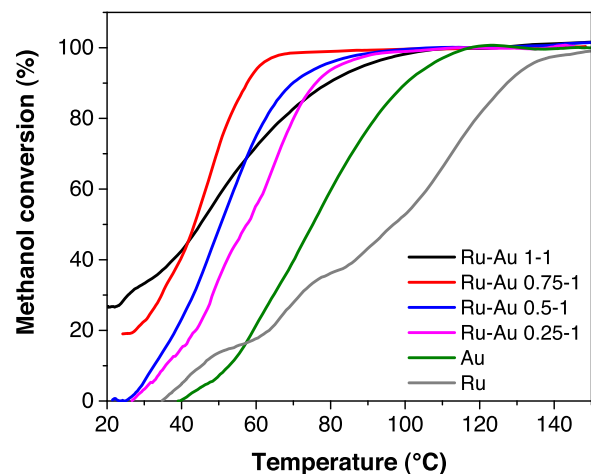


**Fig. 1.** Light-off curves for the oxidation of methanol on monometallic Au and Ru and bimetallic Ru-Au catalysts with different atomic ratio activated in hydrogen at 300 °C.

**Table 1**

Temperatures of 50% and 100% methanol oxidation on the investigated catalysts.

Catalyst	T <sub>50</sub> (°C)	T <sub>100</sub> (°C)
Au	75	118
Ru	97	142
Ru-Au 1-1	45	104
Ru-Au 0.75-1	43	68
Ru-Au 0.5-1	50	91
Ru-Au 0.25-1	58	91

cell was filled with 5% O<sub>2</sub>/He flow (40 mL min $^{-1}$ ) and heated from RT until methanol consumption was achieved (~120 °C). IR spectra were recorded at RT and during the heating (every 10 °C).

Infrared transmission spectra were acquired with a Nicolet 8700 FTIR spectrophotometer equipped with a MCT detector (4 cm $^{-1}$  resolution, 100 scans). Background correction of the spectra was achieved by subtracting the spectra of the clean wafers after the pre-treatment at room temperature.

## 3. Results

### 3.1. Oxidation of methanol

**Fig. 1** shows the light-off curves for the combustion of methanol on the investigated catalysts. Signals obtained by mass spectrometry showed CO<sub>2</sub> and H<sub>2</sub>O to be the only reaction products. **Table 1** summarizes the temperatures required to reach 50% conversion (T<sub>50</sub>) and 100% conversion (T<sub>100</sub>) for each catalyst. The monometallic Ru catalyst began to be active to oxidize methanol at ca. 35 °C, reaching 50% conversion at 97 °C (T<sub>50</sub>) and complete conversion at 142 °C (T<sub>100</sub>). The gold-titania catalyst was more active than the ruthenium one, showing a T<sub>50</sub> at 75 °C and T<sub>100</sub> at 118 °C. In the case of the bimetallic catalysts, the increase in the Ru:Au ratio led progressively to a more active catalyst. The T<sub>50</sub> decreased to 58, 50, 44 and 45 °C for the Ru-Au 0.25-1, 0.5-1, 0.75-1 and 1-1 catalysts, respectively. Moreover, the Ru-Au 1-1 and Ru-Au 0.75-1 samples exhibited 30% and 20% methanol conversion at 25 °C, respectively. This behavior was also observed for the temperature required to reach 100% methanol conversion, except for the Ru-Au 1-1 catalyst, which exhibited the lowest activity, compared to the other bimetallic Ru-Au catalysts. It is important to highlight that the combination of Ru and Au produced more active catalysts in the complete oxidation reaction of methanol, with Ru-Au 0.75-1 catalyst being the most active in the whole temperature reaction range. **Table 2** shows

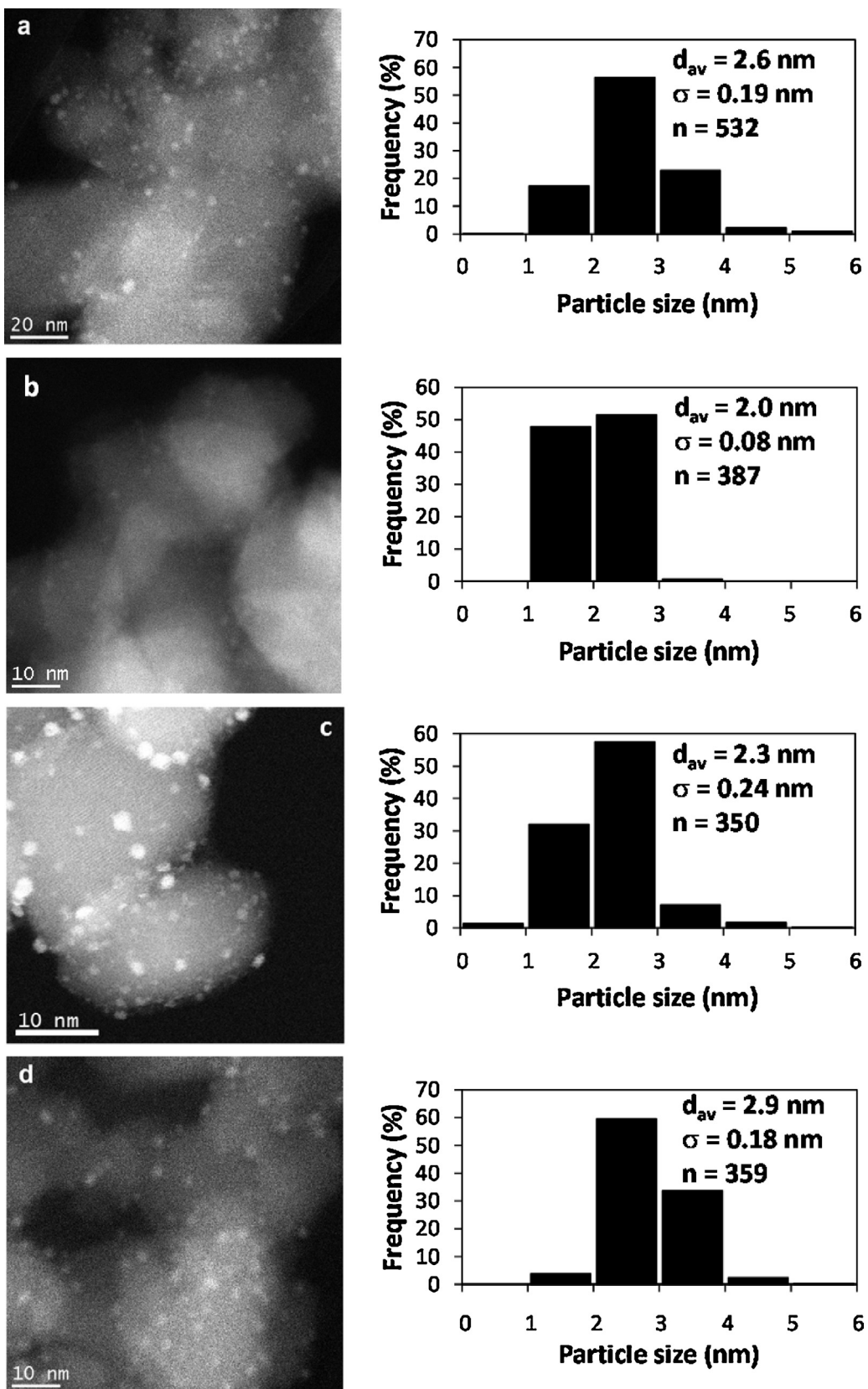


Fig. 2. HAADF images and particle size distributions of the catalysts reduced in hydrogen at 300 °C: a) Au, b) Ru, c) Ru-Au 1-1 and d) Ru-Au 0.75-1.

the specific reaction rates and TOF values for the monometallic Au and Ru catalysts as well as the Ru-Au 0.75-1 bimetallic one calculated in kinetic regime. It can be observed that the reaction rates

of the monometallic catalysts are lower than the one of the Ru-Au 0.75-1 catalyst. Moreover, the TOF calculated for the 0.75-1 catalyst is more than twice higher than the monometallic ones. This result

**Table 2**

Comparison of the reaction rates for  $\text{CH}_3\text{OH}$  oxidation of Au, Ru and Ru-Au 0.75-1 catalysts. The determination of the reaction rate at 60 °C was performed in kinetic regime at conversions lower than 20%.

Catalyst	Dispersion	Reaction rate( $\text{mol}_{\text{CH}_3\text{OH}} \text{g}_{\text{cat}}^{-1} \text{s}^{-1}$ )	TOF( $\text{s}^{-1}$ )
Au	0.44	$5.4 \times 10^{-7}$	0.007
Ru	0.55	$5.5 \times 10^{-7}$	0.006
Ru-Au 0.75-1	0.41	$1.7 \times 10^{-6}$	0.016

confirms the synergistic effect observed in the bimetallic system. It is important to highlight that the combination of Ru and Au produced more active catalysts in the complete oxidation reaction of methanol, with the Ru-Au 0.75-1 catalyst being the most active in the whole temperature reaction range.

### 3.2. Elemental analysis

The theoretical metal loadings for the monometallic catalysts were 3 wt.% Au for Au/TiO<sub>2</sub> and 1.56 wt.% Ru for Ru/TiO<sub>2</sub>, which corresponded to 0.4 at.% for both samples. Table 3 shows the comparison between the nominal and actual metal loadings, together with the results for the bimetallic Ru-Au/TiO<sub>2</sub> catalysts with different atomic ratio. In the case of gold, all the metal was deposited on the support in both the monometallic and bimetallic samples, which is in agreement with former studies on gold catalysts [27,28,31]. Regarding ruthenium, about 90% of metal in solution was deposited, which means that DPU is an accurate method to synthesize Ru catalysts supported on TiO<sub>2</sub>.

### 3.3. Particle size

Fig. 2 shows some selected HAADF images and the particle size distribution for the Au, Ru, Ru-Au 1-1 and Ru-Au 0.75-1 catalysts after activation in H<sub>2</sub> at 300 °C. The average metal particle size is reported in Table 3. The particle size for Au and Ru after thermal treatment was 2.6 and 2 nm, respectively, whereas for the Ru-Au 1-1 and Ru-Au 0.75-1 it was 2.3 and 2.9 nm, respectively. These results indicate that there was no strong difference in the particle size between the monometallic Au catalyst and the bimetallic ones; however, all of them were slightly larger than the monometallic Ru catalyst.

### 3.4. Reducibility of gold and ruthenium in the dried samples

#### 3.4.1. H<sub>2</sub>-TPR characterization

The reducibility of the dried samples was studied by H<sub>2</sub>-TPR (Fig. 3). The results show that the monometallic Au catalyst presented a simple reduction peak between 120 and 175 °C with a maximum at 141 °C, which is ascribed to the reduction of Au<sup>3+</sup> to Au<sup>0</sup> [32,33]. The monometallic Ru catalyst exhibited a peak centered at 103 °C (from 75 to 130 °C) that could be attributed to the reduction of ruthenium species derived from hydrolysis (RuO<sub>x</sub>, RuO<sub>2</sub> amorphous or Ru(OH)<sub>x</sub>) to Ru<sup>0</sup> [34–36]. Another broad peak from 200 to 300 °C, with a maximum at 250 °C was also observed, which could be related to the reduction of Ru(OH)<sub>3</sub> species [34], the partial reduction of TiO<sub>2</sub> surface [37] or the reduction of RuO<sub>2</sub> [38]. The bimetallic Ru-Au catalysts showed a peak located at 106, 114, 112 and 119 °C for the 1-1, 0.75-1, 0.5-1 and 0.25-1 Ru-Au atomic ratio, respectively, attributed to the reduction of the before mentioned Ru and Au species. It is interesting to note that the maximum of the peak of the bimetallic samples was between the maxima of the monometallic Ru and Au catalysts and that these peaks were shifted to higher temperature when the Au atomic ratio was increased. On the other hand, the Ru-Au 0.25-1 catalyst showed a shoulder at ~130 °C, related to the reduction of gold species.

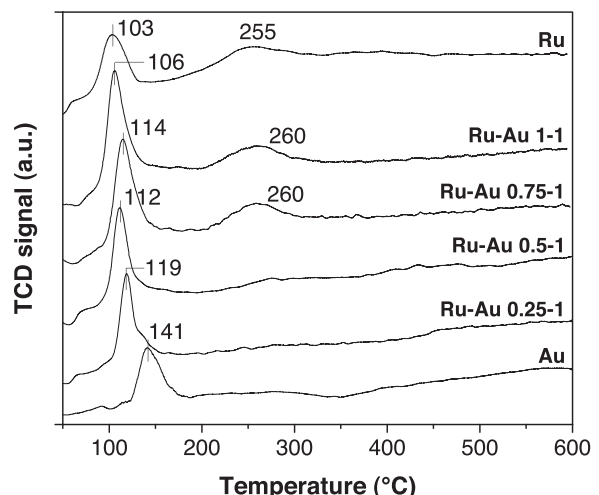


Fig. 3. H<sub>2</sub>-TPR profiles of dried bimetallic Ru-Au catalysts, including monometallic Ru and Au catalysts for comparison.

The presence of the first peak suggests some kind of interaction between Au and Ru, and a promotion of gold reduction by ruthenium. In the Ru-Au 0.25-1 sample, the amount of Ru might not be enough to promote the reducibility of Au. In addition, the catalysts with high Ru loading exhibited also the second broad peak between 200 and 300 °C.

#### 3.4.2. UV-vis characterization

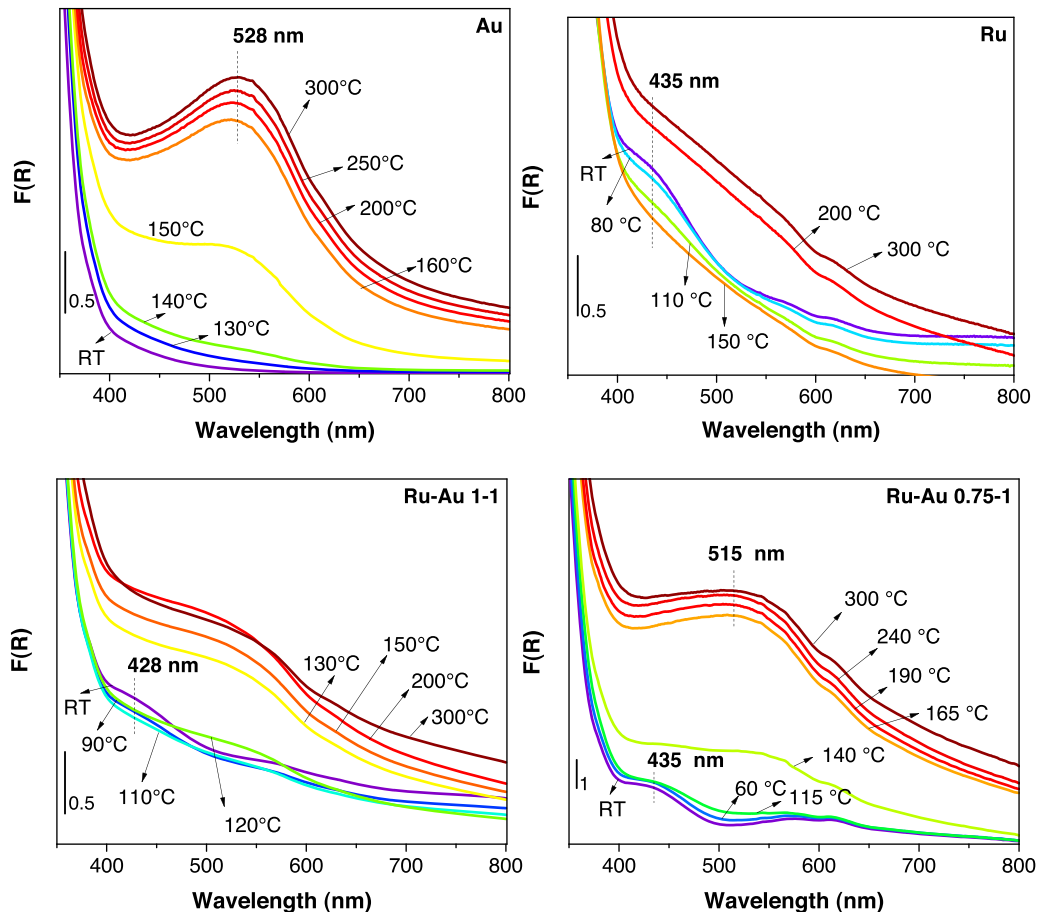
The Au, Ru, Ru-Au 1-1 and Ru-Au 0.75-1 samples were analyzed by *in situ* UV-vis spectroscopy under H<sub>2</sub>/Ar flow from RT to 300 °C (Fig. 4). The monometallic Au catalyst (Fig. 4a) developed a characteristic broad band between 400–800 nm at increasing temperature because of the surface plasmon resonance (SPR) of metallic gold nanoparticles [39,40]. This band started to be visible and increased from 150 °C, reaching a maximum intensity at 300 °C, located at 528 nm. Fig. 4b shows the UV-vis spectrum of the Ru sample, a weak and broad absorption band at ~430 nm was present at room temperature, which could be ascribed to a d-d transition band [41]. With the increase in temperature, this band lost intensity and a continuous band in the visible region, characteristic of Ru<sup>0</sup> nanoparticles, was observed [42–44].

The initial spectra from the bimetallic Ru-Au 1-1 and Ru-Au 0.75-1 samples are shown in Fig. 4c and d, respectively. The adsorption band at ~430 nm was also observed at RT; during the increase in temperature, this band disappeared as in the monometallic Ru catalyst, indicating the reduction of the Ru species, and a new band started to evolve at 120 °C, which is related to the SPR of metallic gold nanoparticles. Interestingly, the evolution of the gold plasmon band started at lower temperatures in the bimetallic catalysts than in the monometallic Au sample. This result indicates that gold nanoparticles are formed at lower temperatures in the presence of ruthenium, in agreement with H<sub>2</sub>-TPR profiles. Moreover, the shape of the absorption band in the bimetallic catalysts was different to that in the monometallic Ru and Au samples, showing a lower intensity, and shifted to a lower wavelength. In the Ru-Au 0.75-1 sample, the plasmon band was blue-shifted to ~515 nm, whereas in the Ru-Au 1-1 the sample, the band was less defined at around 510 nm. It is known that the shape and position of the plasmon band depend on the particle size, shape and surrounding environment [45–47]. Note here that the Au loading and particle size distribution were similar in both the Ru-Au 1-1 and the Ru-Au 0.75-1 samples. Then, these results also point out to a close interaction between gold and ruthenium in the bimetallic catalysts. Kumar et al. [44] prepared Au-Ru bimetallic nanoparticles by sono-

**Table 3**

Composition and average metal particle size of the catalysts studied.

Catalyst	Au (wt.%)		Ru (wt.%)		Atomic ratio actual Ru/Au	Average particle size (nm)
	Theoretical	Actual	Theoretical	Actual		
Au	3	3.2	–	–	–	2.6
Ru	–	–	1.56	1.5	–	2.0
Ru-Au 1-1	3	3.1	1.56	1.4	0.88	2.3
Ru-Au 0.75-1	3	3.1	1.19	1.1	0.69	2.9
Ru-Au 0.5-1	3	3.2	0.79	0.7	0.43	Not measured
Ru-Au 0.25-1	3	3.2	0.4	0.4	0.24	Not measured

**Fig. 4.** UV-vis spectra of samples reduced *in situ* under hydrogen at increasing temperatures.

chemical reduction followed by UV-vis spectroscopy and observed a slight decrease in the SPR originated by a Ru layer formed on the Au nanoparticles. Thus, the UV-vis spectra of bimetallic catalysts suggest that the interaction between both metals could be ascribed to a partial covering of gold nanoparticle by Ru.

### 3.5. XPS results

To obtain electronic information of the activated catalysts, XPS analysis were performed. The observed Au 4f<sub>7/2</sub> and Ru 3d<sub>5/2</sub> binding energies for the monometallic references and the bimetallic Ru-Au 0.75-1 catalyst are shown in **Fig. 5** and reported in **Table 4**. The characteristic Au 4f<sub>7/2</sub> photoelectron peak, located at BE values between 84.3 and 84.7 eV, because of the presence of metallic gold [48–50], is observed on both mono and bimetallic catalysts (**Fig. 5a**). The shift of the Au 4f<sub>7/2</sub> core-level peak to higher energies, relative to the bulk value of 84.0 eV, has been attributed to particle size effects [51]. Additionally, in the Ru-Au catalyst, some features are observed at much higher BE, that is 89.39 and 86.40 eV. These

peaks are in agreement with the presence of partially oxidized gold species [48].

The XPS analysis in the Ru 3d region of the Ru and Ru-Au catalyst shows two couples of peaks that can be assigned to two different species (**Fig. 5b**). Peaks close to 284.5 eV and 280.7 are assigned to metallic ruthenium [52,53]. The couple of bands at around 286.5 and 282.0 indicate that ruthenium-oxidized species are present at the surface of the particles. These species could be assigned to RuO<sub>2</sub>. There is no fundamental difference between monometallic and the bimetallic one in this XPS region.

### 3.6. Composition of the particles

To get further insight into the nanometric interaction between both metals, a detailed analysis of the Ru-Au 1-1 catalyst activated in hydrogen at 300 °C was performed by HAADF-STEM and STEM-EDS employing an aberration corrected STEM. A STEM operated in the mode in which the scattered electrons are collected by means of a HAADF detector forms a Z-contrast image. Because of

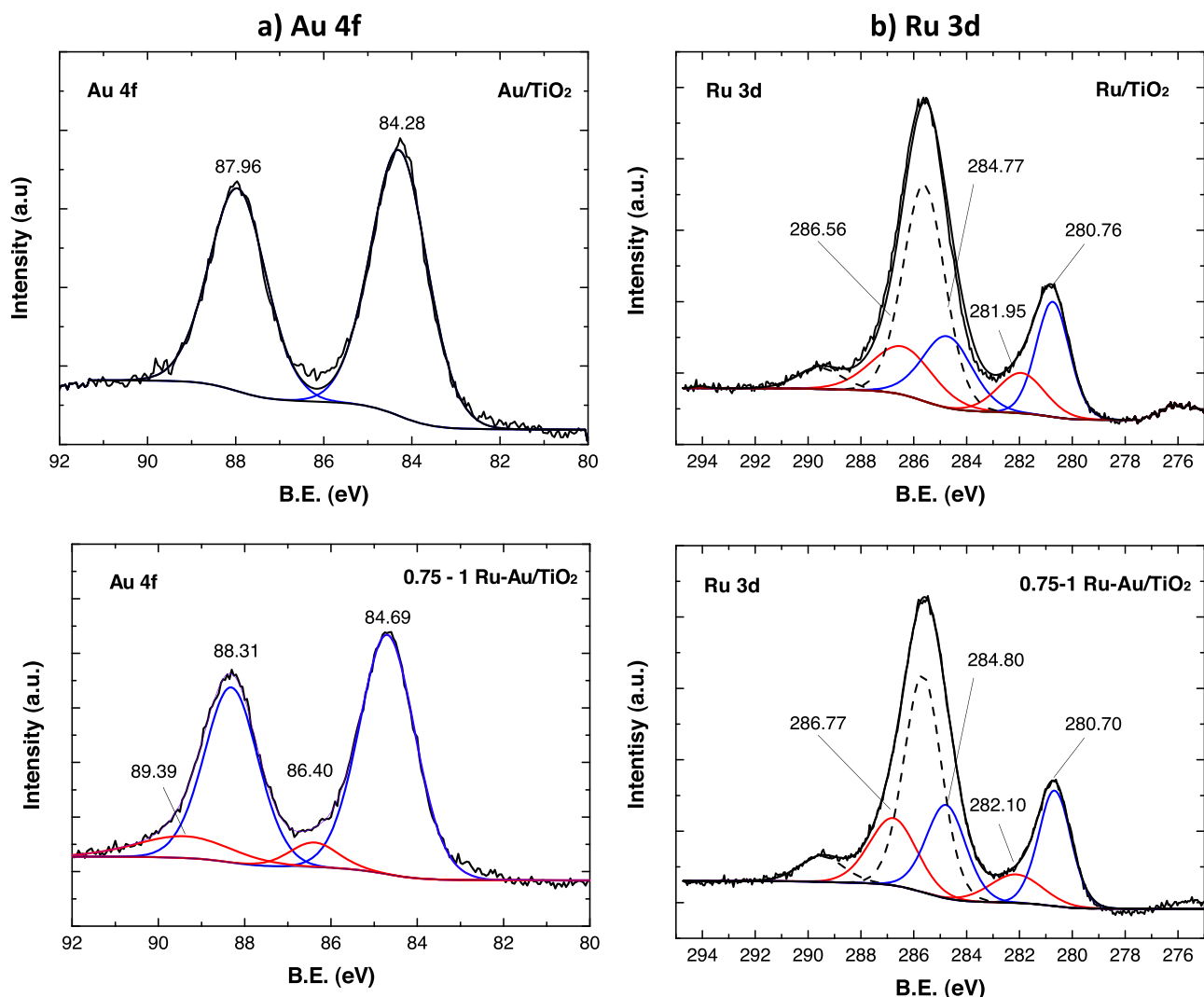


**Fig. 5.** XPS spectra in the 4f region of gold (a) and 3d of ruthenium (b) for the monometallic Au/TiO<sub>2</sub>, Ru/TiO<sub>2</sub> and bimetallic 0.75-1 Ru-Au/TiO<sub>2</sub> catalysts pre-reduced in situ under flowing H<sub>2</sub> at 300 °C. Dash lines correspond to C 1s signals.

**Table 4**

Binding energy values of gold and ruthenium phases on the Au, Ru and Ru-Au 0.75-1 catalysts determined by XPS measurements.

Catalyst	Au 4f <sub>7/2</sub> (eV)		Ru 3d <sub>5/2</sub> (eV)	
	Au (0)	Au(δ+)	Ru (0)	RuO <sub>2</sub>
Au	87.96	84.28		
Ru			284.77	280.76
Ru-Au 0.75-1	88.31	84.69	86.40	286.56 284.80 282.10 280.70

the inherent nature of the Z-contrast HAADF-STEM mode, where the image intensity is approximately proportional to the square of the atomic number (Z<sup>2</sup>), Au (Z = 79) and Ru (Z = 44) can easily be distinguished by the intensity differences [54,55]. Consequently, Au particles appear brighter than Ru particles in the Z-contrast STEM images, as shown in Figs. 6 a and 7a. According to these images, the Ru-Au 1-1 catalyst is made up of small Ru monometallic particles (~2 nm) and particles composed of Ru and Au in interaction, forming different structures. The EDS mapping in Fig. 6b suggests that these bimetallic structures consists of two parts, one rich in Au and another one rich in Ru (a kind of Janus structures). The EDS line profile of other structures show gold cores partially covered by Ru (Fig. 7b). These results confirm the interaction between Au and Ru in the bimetallic particles.

### 3.7. Surface composition of the catalysts by CO-DRIFTS

The surface composition of the particles in the bimetallic Ru-Au 1-1 and Ru-Au 0.75-1 samples was studied using CO as a probe molecule by DRIFTS after *in situ* activation in hydrogen performed at 300 °C. The monometallic Au and Ru samples were also analyzed for comparison.

The adsorption of CO in the Au catalyst (Fig. 8) led first to the apparition of a band at 2100 cm<sup>-1</sup> attributed to CO adsorbed on low-coordinated surface Au<sup>0</sup> atoms [56,57]. This band disappeared slightly under the constant exposure to CO and a new one started to evolve at 2040 cm<sup>-1</sup>, which was ascribed to CO adsorbed on negatively-charged gold sites (Au<sup>δ-</sup>) [57–61] as a result of the creation of new adsorption sites due to the reconstruction of the gold nanoparticles under CO exposure [62].

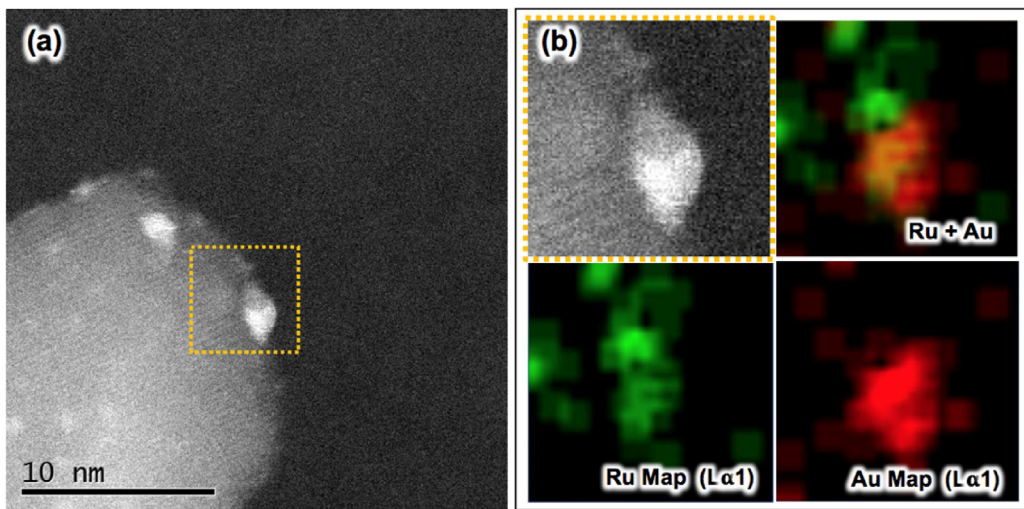


**Fig. 6.** (a) HAADF-STEM image of the catalysts Ru-Au 1-1, showing Ru-Au metals in interaction; (b) component maps.

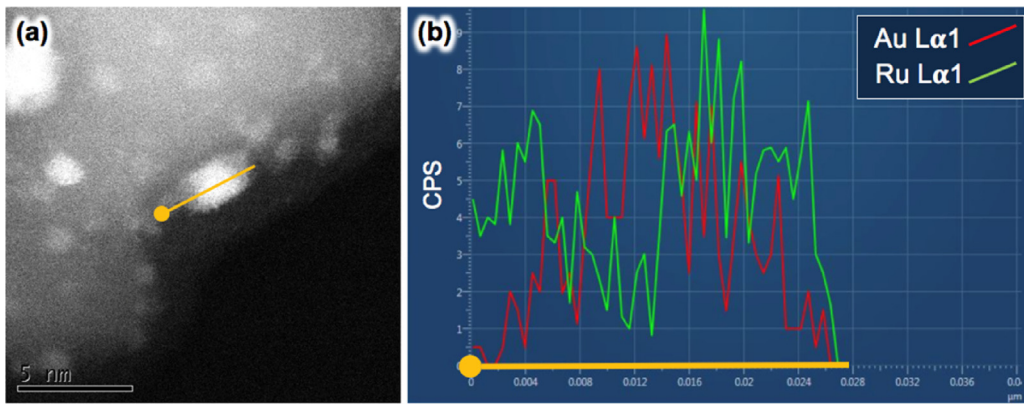


**Fig. 7.** (a) HAADF-STEM image of the catalyst Ru-Au 1-1, showing Ru-Au metals in interaction; (b) EDS line profile.

The monometallic Ru catalyst (Fig. 8) initially exhibited a complex spectrum which was characterized by a single band located at  $2128\text{ cm}^{-1}$  and an intense broad band with a long tail in the  $2100\text{--}1900\text{ cm}^{-1}$  region; in addition, absorption bands at  $2059$  and  $1993\text{ cm}^{-1}$  as well as a shoulder at  $2030\text{ cm}^{-1}$  were detected. With the continue exposition to CO, all the bands increased in intensity and the band at  $1993\text{ cm}^{-1}$  became more defined. The high frequency bands situated at  $2128$  and  $2059\text{ cm}^{-1}$  are attributed to the adsorption of mult carbonyl species on partially oxidized Ru sites ( $\text{Ru}^{n+}(\text{CO})_x$ ) [63–66]. The band at  $2059\text{ cm}^{-1}$  may also contain contributions from dicarbonyl species adsorbed on  $\text{Ru}^0$  ( $\text{Ru}^0\text{--}(\text{CO})_2$ ), which has been observed between  $2062$  and  $2049\text{ cm}^{-1}$  [63,67]. The shoulder at  $2030\text{ cm}^{-1}$  is attributed to linear  $\text{Ru}^0\text{-CO}$  species and the position of this band depends strongly on the CO coverage [64]. The band at  $1993\text{ cm}^{-1}$  is frequently ascribed to linear adsorbed CO on isolated  $\text{Ru}^0$  sites surrounded by partially oxidized  $\text{Ru}^{n+}$  sites [63,66], and it may contain contributions from  $\text{Ru}^{n+}\text{-CO}$  species [66]. There is also an additional contribution from dicarbonyl species formed on  $\text{Ru}^0$  in this position, according to the results reported by Chin et al. [63]. The long tail in the low frequency band is attributed to a bridged-bonded CO of the  $\text{Ru}_2^0\text{-CO}$  type [63,67]. There are other attributions proposed for the band at  $1993\text{ cm}^{-1}$  as the CO adsorption on Ru metal sites that interact strongly with the metal oxide support, as well as CO species adsorbed on Ru sites located at the metal support interface [66].

The initial spectra from the bimetallic Ru-Au 1-1 and Ru-Au 0.75-1 catalysts (Fig. 8) exhibited a complex broad band from  $2140$

to  $1900\text{ cm}^{-1}$  with peaks located at  $2061$ ,  $2029$  and  $1992\text{ cm}^{-1}$  for the Ru-Au 1-1 catalyst, and  $2066$ ,  $2033$  and  $1993\text{ cm}^{-1}$  for the Ru-Au 0.75-1 one. However, compared to the monometallic Ru catalyst, the high frequency band at  $\sim 2130\text{ cm}^{-1}$ , attributed to  $\text{Ru}^{n+}(\text{CO})_x$  species in bimetallic samples, is not well defined because of the overlap with the shoulder at  $\sim 2100\text{ cm}^{-1}$ . That is due to the contribution of CO adsorption on the metallic Au sites, whose band seems to be red-shifted showing a lower intensity than that of the monometallic Au sample. Under continuous CO exposure, the shoulder related to  $\text{Au}^0\text{-CO}$  decreased in intensity, as in the monometallic Au sample, whereas the bands related to Ru enhanced their intensity.

It is important to note that the intensity of the bands related to the CO adsorption on Ru sites in the Ru-Au 0.75-1 catalysts are lower than in the monometallic Ru and the Ru-Au 1-1 samples (Fig. 9), as well as the presence of the shoulder at  $2100\text{ cm}^{-1}$  with lower intensity indicating a shift in the  $\text{Au}^0\text{-CO}$  band in the bimetallic samples. These facts could be related to the interaction between Ru and Au, which decreased the number of adsorption sites on the surface and it also indicated a change in the nature of gold sites. This idea is also supported by TEM results, which showed different Ru-Au mixed structures. We cannot discard the possibility that the lower intensity of the bands in the Ru-Au 0.75-1 catalyst is due to the decrease of Ru loading.

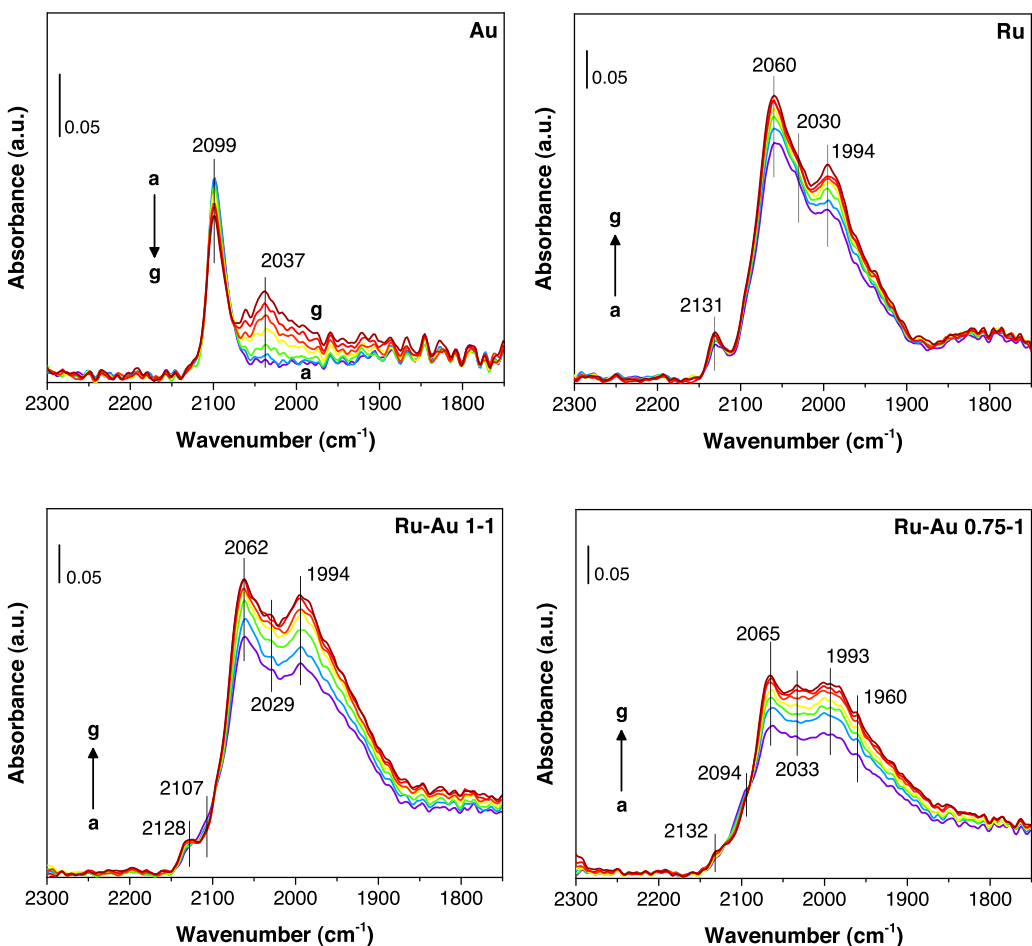


**Fig. 8.** DRIFT spectra recorded at RT of CO adsorbed on catalysts after *in situ* activation in hydrogen at 300 °C, at different times: (a → g) 5, 10, 20, 30, 40, 50 and 60 min.

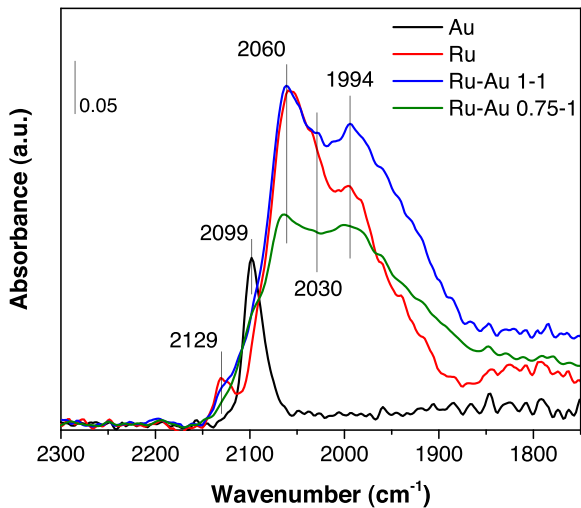


**Fig. 9.** Comparison of the DRIFT-CO spectra of monometallic Ru and Au and bimetallic Ru-Au 1-1 and Ru-Au 0.75-1 at RT.

### 3.8. Oxidation of methanol followed by FTIR

#### 3.8.1. Adsorption of methanol

The adsorption of methanol was recorded by FTIR to elucidate the species adsorbed on the catalysts. Fig. 10 shows the spectra after the adsorption of methanol at RT and subsequent evacuation of the Ru and Au monometallic catalysts, as well as that of

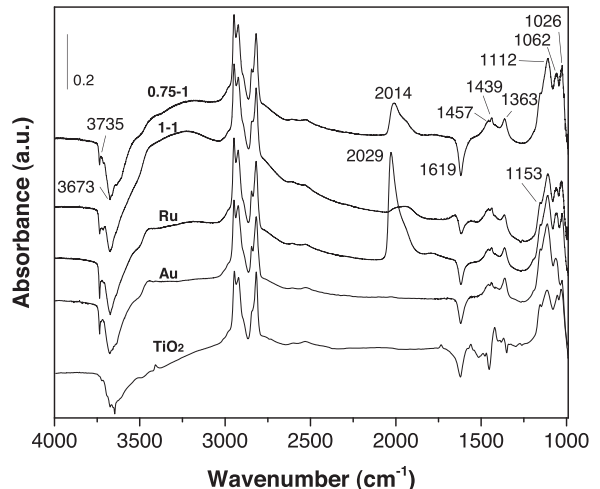


**Fig. 10.** IR spectra after CH<sub>3</sub>OH adsorption at RT on Au, Ru, Ru-Au 1-1 and Ru-Au 0.75-1 catalysts activated under H<sub>2</sub> at 300 °C.

the bimetallic Ru-Au 1-1 and Ru-Au 0.75-1 catalysts. The IR spectra recorded prior to CH<sub>3</sub>OH adsorption were subtracted from the spectra of methanol-exposed surfaces in order to isolate the surface signals arising from the chemisorption of methanol. For comparison purposes, the spectrum of methanol adsorbed on the bare TiO<sub>2</sub> support was also included. After exposure to methanol, molecularly adsorbed methanol (CH<sub>3</sub>OH<sub>s</sub>) and methoxy (CH<sub>3</sub>O<sub>s</sub>) species were formed on the surface of TiO<sub>2</sub>. The later surface groups were pro-

duced by a reaction with OH on the surface of the metallic oxides with the elimination of water molecules [15,68–71]. This process is clearly observed in the 3760–3500 cm<sup>−1</sup> region that exhibits a broad negative band, related to the depletion of the superficial hydroxyl species on TiO<sub>2</sub>, as well as a negative peak at 1620 cm<sup>−1</sup>, which is characteristic of  $\delta(\text{H}_2\text{O})$  vibrational mode. The  $\nu(\text{CH})$  stretching mode (3100–1700 cm<sup>−1</sup>) displayed peaks related to the formation of methoxy and methanol species molecularly adsorbed on the support; nevertheless, because of the high overlapping of the several modes of both species, this region is not useful for the identification of adsorbed species, whereas the  $\nu(\text{CO})$  mode region (1200–1000 cm<sup>−1</sup>) is more appropriate for this purpose.

The bands at 1457, 1439 and 1153 cm<sup>−1</sup> are attributed to methoxy species (CH<sub>3</sub>O<sub>S</sub>) with  $\delta_{\text{as}}(\text{CH}_3)$ ,  $\delta_{\text{s}}(\text{CH}_3)$  and  $\rho(\text{CH}_3)$  vibrational modes, respectively, whereas the band at 1363 cm<sup>−1</sup> could be ascribed to carbonates. In the  $\nu(\text{CO})$  region, there are signals at 1112 and 1062 cm<sup>−1</sup> related to mono and bidentate methoxy species, whereas the band at 1026 cm<sup>−1</sup> is due to methanol in gaseous phase [68,72,73].

The catalysts containing ruthenium also exhibited a single peak at ~2029 cm<sup>−1</sup>, which is ascribed to CO adsorbed on the metallic sites of Ru (Ru<sup>0</sup>-CO). Different studies have demonstrated that methanol is completely dehydrogenated on Ru(0001) surfaces at temperatures lower than RT, producing adsorbed hydrogen and carbon monoxide species [74–76]. The intensity of the Ru<sup>0</sup>-CO peak was much higher for the monometallic Ru catalyst, whereas the intensity was less pronounced in the bimetallic Ru-Au 1-1 and Ru-Au 0.75-1 catalysts, probably because of the interaction between Au and Ru, which decreased the Ru adsorption sites.

### 3.8.2. Temperature-programmed oxidation of adsorbed methanol

Temperature-programmed oxidation of adsorbed methanol (TPSR) experiments were performed after the adsorption of methanol under a dynamic flow of 5% O<sub>2</sub>/He in the cell. Infrared spectra were acquired at different temperatures to detect the evolution of the species involved during the oxidation of methanol. The catalysts analyzed were the monometallic and the bimetallic Ru-Au 1-1 and Ru-Au 0.75-1 ones shown in Fig. 11. The evolution of the intensity of some of the bands as a function of the temperature is depicted in Fig. 12.

The admission of oxygen into the cell and the increase in temperature in the Au catalyst (Figs. 11a and 12a) led to the continuing decrease of methoxy species with mono and bidentate coordination at 1113 and 1060 cm<sup>−1</sup>, respectively. In addition, the evolution of the bands at 1587, 1359, 1558 and 1380 cm<sup>−1</sup>, which are attributed to the vibrational asymmetric and symmetric  $\nu(\text{OCO})$  mode (the first two for bidentate and the last two for bridged coordination, respectively [73]), was also observed. The highest intensity of formates was reached at 40 °C remaining almost constant at 50 °C and, upon continuous heating, they started to be consumed (Fig. 12a). The depletion was a little faster for bidentate formate species than for bridged ones, indicating that the first ones were more active. On the other hand, the intensity of monodentate methoxy decreased faster than for bidentate species (Fig. 12a). This consumption could be related to the production of formates (until 40 °C) and the complete oxidation of methoxy species. The band related to CO<sub>2</sub> production (2349 cm<sup>−1</sup>) started to evolve at 40 °C and it was enhanced by increasing the temperature, which is in agreement with mass spectrometry results. At this temperature, formates could participate in the complete oxidation to produce CO<sub>2</sub>, which is in agreement with the decrease of the intensity of the band ascribed to the formates at 50 °C, the increase in CO<sub>2</sub> production (60 °C) and the increase in the band of water (1620 cm<sup>−1</sup>). It must also be noted that the intensity of the OH group in the 3750–3500 cm<sup>−1</sup> region, increased at ~50 °C, which indicates the restoration of the hydroxyl species adsorbed on titania, as an inter-

mediate from the oxidation of formates. These temperatures are in agreement with the results of the oxidation of methanol shown in Fig. 1.

Fig. 11b shows the FTIR spectra for the monometallic Ru catalyst after the introduction of oxygen. The rise in the temperature led to the continuous and slow consumption of the methoxy species with mono and bidentate coordination, peaks at 1113 and 1059 cm<sup>−1</sup>, respectively. Next, the immediate appearance of bidentate and bridged formate species in an overlapped peak at 1576 cm<sup>−1</sup>, containing the asymmetric vibrational modes  $\nu(\text{OCO})$  at ~1587 and ~1556 cm<sup>−1</sup>, and the symmetric ones at 1357 and 1380 cm<sup>−1</sup>, was observed. These bands increased in intensity reaching a maximum at 80 °C, and then they were consumed. Additionally, the peak located at 2029 cm<sup>−1</sup>, attributed to CO adsorbed on the metallic Ru sites was consumed and split in two new bands at 2057 and 1996 cm<sup>−1</sup> (Ru<sup>0</sup>-(CO)<sub>2</sub>) when the oxygen flow was introduced in the cell (Figs. 11b and 12b). The consumption of the Ru<sup>0</sup>-CO could be related to the production of CO<sub>2</sub> (band at 2349 cm<sup>−1</sup>) at RT. The presence of a small band located at 2118 cm<sup>−1</sup> (Ru<sup>n+</sup>(CO)<sub>x</sub>) indicates the partial oxidation of Ru caused by the presence of oxygen. With continuous annealing, the intensity of the split band decreased slightly in parallel with the formation of a very small quantity of CO<sub>2</sub>. Finally, the increase in CO<sub>2</sub> production was achieved at 80 °C, which coincides with the fast depletion of formates as well as of the dicarbonyl species. Note here that the consumption of formates and the production of CO<sub>2</sub> at temperatures above 80 °C (mass spectroscopy results) is in agreement with the lower catalytic activity, as compared to pure gold, reported before for the Ru/TiO<sub>2</sub> catalyst.

The FTIR spectra of the Ru-Au 1-1 and Ru-Au 0.75-1 catalysts are shown in Fig. 11c and d, respectively. Both samples showed a similar behavior when oxygen was admitted into the cell and the temperature was increased. Firstly, the methoxy species in mono- (~1107 cm<sup>−1</sup>) and bidentate (~1056 cm<sup>−1</sup>) coordination lost intensity from RT. It was noticed that the monodentate coordination was more reactive than the bidentate one in the methoxy species because at 50 °C the second one was still present, whereas the monodentate had completely disappeared (Fig. 12c and d). The formation of CO<sub>2</sub> was instantaneous at RT and its continuous production when the temperature was increased was consistent with the catalytic test of the oxidation of methanol and the mass spectrometry results. Moreover, formate species were also produced after the introduction of oxygen. The asymmetric  $\nu(\text{OCO})$  vibrational mode revealed an overlapped peak in the 1600–1500 cm<sup>−1</sup> region with a maxima at ~1560 cm<sup>−1</sup>, which contained the contribution of bidentate (~1580 cm<sup>−1</sup>) and bridged (~1557 cm<sup>−1</sup>) formate species. The symmetric  $\nu(\text{OCO})$  vibrational mode was observed at ~1380 and ~1358 cm<sup>−1</sup> for the bidentate and bridged coordination. The maximum production of formates was reached at 40 °C (Fig. 12c and d) and their intensity was much lower than that of the monometallic Ru catalyst; this fact could result from the interaction between Ru and Au in the bimetallic samples. Then, the intensity of both bidentate and bridged species, started to decline in parallel (Fig. 12c and d). In the monometallic Au catalyst, the bidentate configuration of formates was more reactive and disappeared faster than the bridged species; however, this behavior was not observed in bimetallic samples, probably because the bidentate formates were found between the  $\delta(\text{H}_2\text{O})$  and the bridged formate species, which contributed to the intensity. The restoration of the OH surface caused by the oxidation of formates was also observed in both samples.

As in the monometallic Ru catalyst, the complete dehydrogenation of methanol could be produced in the bimetallic Ru-Au 1-1 and Ru-Au 0.75-1 catalysts, producing CO adsorbed on the Ru metallic sites (band located at ~2014 cm<sup>−1</sup>); nevertheless, although the intensity was lower than in the monometallic Ru catalyst

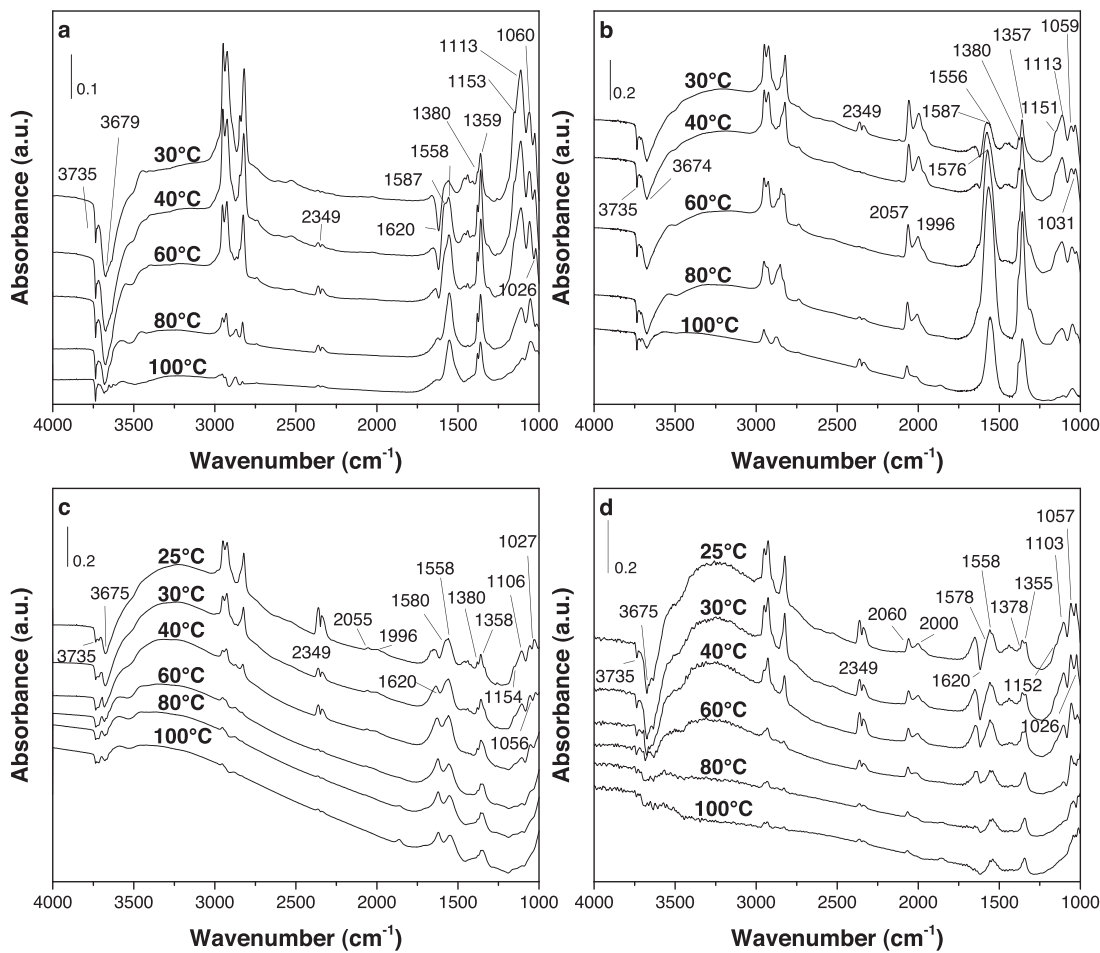


**Fig. 11.** IR spectra with dynamic 5%O<sub>2</sub>/He flow at different temperatures on a) Au, b) Ru, c) Ru-Au 1-1 and d) Ru-Au 0.75-1 catalysts.

(Fig. 13a), the split and decrease in this band was evident after oxygen introduction (Fig. 13b) which may be related to the early production of CO<sub>2</sub> (2349 cm<sup>-1</sup>) at RT, as it was previously proposed for the monometallic Ru catalyst. The new bands formed because of the split of the Ru<sup>0</sup>-CO band (Fig. 13b), located at ~2057 cm<sup>-1</sup> and ~1996 cm<sup>-1</sup>, are characteristic of the Ru<sup>0</sup>-(CO)<sub>2</sub> species. The absence of the band at ~2118 cm<sup>-1</sup> indicated that there was not oxidation of the Ru<sup>0</sup> sites caused by the exposition to oxygen (Fig. 13b).

In addition, the comparison between the DRIFT spectra of the monometallic Ru catalyst and the FTIR spectra of the mono and bimetallic catalysts recorded after the adsorption of methanol at RT (Fig. 13a) shows the presence of narrower peaks ascribed to the adsorption of CO on the metallic Ru sites in the bimetallic samples, indicating the absence of Ru<sup>n+</sup> sites. After oxygen exposition (Fig. 13b), a band at 2118 cm<sup>-1</sup> appeared only in the monometallic Ru catalyst, whereas in the bimetallic catalysts was absent, even during heating, which means that the combination of Ru and Au prevented the reoxidation of Ru caused by the oxygen exposition.

#### 4. Discussion

The sequential deposition-precipitation with urea method allows to produce bimetallic Ru-Au particles with different structures. As it is known, Ru and Au are immiscible metals in bulk state [77]; however, when they are in the nanoscale, both metals may interact with each other, forming bimetallic particles [22,23]. The STEM-EDS analysis (Figs. 6 and 7) shows that it is possible to produce bimetallic structures by employing this method, in which Au

and Ru are in contact. The interaction between both metals is also supported by other characterization techniques. The TPR profiles exhibit only a reduction peak that is located between the two maxima of the monometallic Ru and Au catalysts, which means that the addition of Ru promotes the reducibility of Au compared to the monometallic Au sample. These results are consistent with the UV-vis spectra from the bimetallic catalysts (Fig. 4), which show that the apparition and evolution of the SPR of Au starts at a lower temperature than in the monometallic Au catalyst, which indicates the earlier formation of gold nanoparticles as well as changes in the shape of the SPR, which shows an interaction between Au and Ru. In addition, both characterizations show that ruthenium and gold are completely reduced at 300 °C. The XPS results also indicate some changes in the 4f<sub>7/2</sub> BE related to the Au species (Table 4), showing the presence of oxidized gold despite performing the thermal treatment at 300 °C in H<sub>2</sub>. On the other hand, the DRIFT spectra also reveal the presence of bands of Au<sup>0</sup>-CO, Ru<sup>0</sup>-CO and Ru<sup>0</sup>-(CO)<sub>2</sub> in the bimetallic Ru-Au 1-1 and Ru-Au 0.75-1 catalysts (Fig. 8), which confirms the reduction of the nanoparticles. The interaction between Ru and Au in the bimetallic catalysts can also be confirmed by DRIFT analysis because of the decrease and shift in the band of Au<sup>0</sup>-CO (~2100 cm<sup>-1</sup>) in the bimetallic samples and the bands related to CO adsorbed on different Ru sites (2056 and 1995 cm<sup>-1</sup>) in the Ru-Au 0.75-1 catalyst at RT (Fig. 9).

It is known that the O<sub>2</sub>/CH<sub>3</sub>OH molar ratio and the temperature of reaction have an important effect on the distribution of products in the total oxidation of methanol [17,24,68]. At the reaction conditions used in this work, an excess of oxygen was employed to simulate the concentration in air, in this way the results of mass

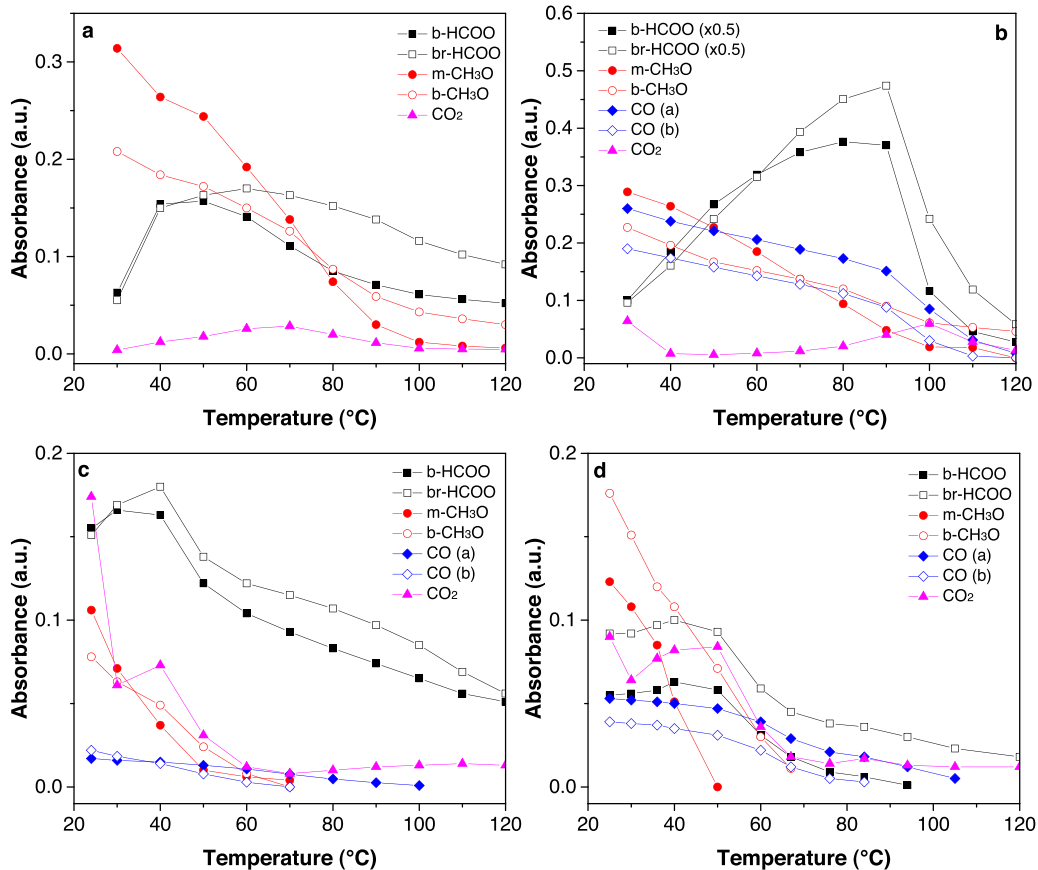


**Fig. 12.** Evolution of the intensity of the IR bands of the surface species on a) Au, b) Ru, c) Ru-Au 1-1 and d) Ru-Au 0.75-1 catalysts, with dynamic 5%O<sub>2</sub>/He flow: b-HCOO [ $\nu_{as}(OCO) = 1587\text{ cm}^{-1}$ ], br-HCOO [ $\nu_{as}(OCO) = 1558\text{ cm}^{-1}$ ], m-CH<sub>3</sub>O [ $\nu(CO) = 1112\text{ cm}^{-1}$ ], b-CH<sub>3</sub>O [ $\nu(CO) = 1060\text{ cm}^{-1}$ ], CO<sub>(a)</sub> [ $\nu(CO) = 2057\text{ cm}^{-1}$ ], CO<sub>(b)</sub> [ $\nu(CO) = 1996\text{ cm}^{-1}$ ], CO<sub>2</sub> [ $\nu(CO) = 2349\text{ cm}^{-1}$ ].

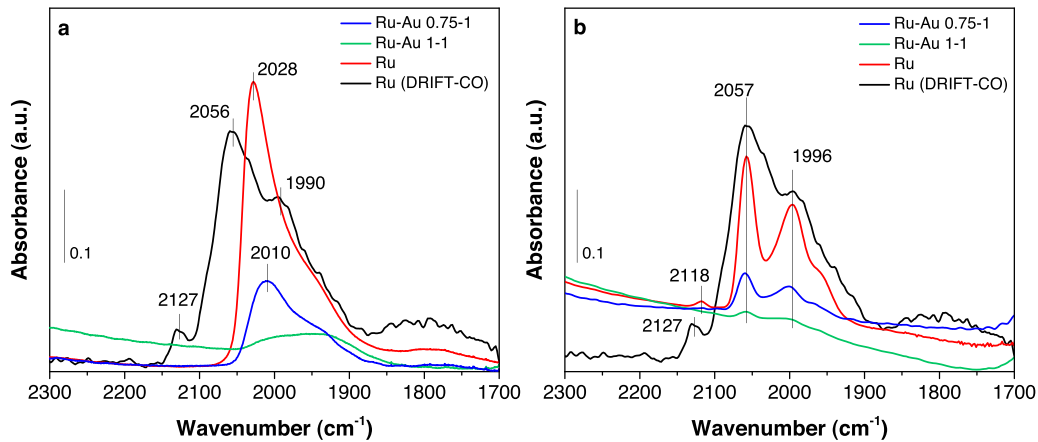


**Fig. 13.** FTIR spectra in the 2300 cm<sup>-1</sup>–1700 cm<sup>-1</sup> region after the adsorption of methanol on the monometallic Ru and bimetallic 0.75-1 and 1-1 Ru-Au catalysts: a) prior to the introduction of oxygen in the cell, and b) after the introduction of oxygen in the cell, at RT. The DRIFT-CO spectra of the monometallic Ru catalyst is also shown for comparison.

spectrometry reveal only the presence of CO<sub>2</sub> and H<sub>2</sub>O as reaction products in all the catalysts studied. According to the results of the catalytic activity in the oxidation of methanol, the addition of Ru to the Au samples generates more active catalysts (Fig. 1). As shown in Table 1, the temperature for both 50% and 100% methanol conversion is lower for the bimetallic catalysts than that for the monometallic Ru and Au ones. Particularly, the Ru-Au 0.75-1 catalyst exhibited a synergistic effect in the low temperature region (RT to 60 °C), which is supported by the TOF values (Table 2). In

accordance with different studies, the interaction between Ru and Au on supported oxides has a synergistic effect on different oxidation reactions, such as the production of H<sub>2</sub> by partial oxidation of methanol [24] and the total oxidation of methanol [25]. Sreethawong et al. [25] tested bimetallic Ru-Au catalysts supported on SiO<sub>2</sub> (24–45 nm) in the oxidation of methanol under reaction conditions similar to those used in this work and they found better catalytic properties in the bimetallic samples than in the monometallic ones; nonetheless, the temperatures for 50% conversion in the bimetallic

catalysts were much higher (>160 °C) than those reported in this work (<60 °C). The lower  $T_{50}$  obtained in the present work can be related to the small particle size obtained in the bimetallic catalysts (~3 nm), which suggests that the particle size is also an important parameter contributing to the superior catalytic behavior. According to the results obtained during the *in situ* FTIR investigation of the oxidation of pre-adsorbed methanol, the production of formates and their oxidation to  $\text{CO}_2$  was promoted in the bimetallic samples. The activation of oxygen at the interface of Au particles with the support has been suggested as a key step for CO and also for the oxidation of methanol [15,17,19]. A similar behavior was reported in the case of bimetallic Au-Ag/TiO<sub>2</sub> catalysts for CO oxidation [31], where it has been proposed that oxygen shows higher affinity to silver than for gold. Moreover, a theoretical and experimental study of a Ru(001) substrate with a submonolayer of Au performed by Kuhn et al. [78] showed that the bonding interactions between Au and Ru involve a redistribution of charge around the metal centers and the formation of interface states. Therefore, in the bimetallic Ru-Au catalysts, oxygen could be activated more easily on the Ru sites and create new and more active gold adsorption sites as revealed by CO adsorption by DRIFTS.

Concerning the FTIR spectra of the adsorption of methanol and the  $\text{CH}_3\text{OH} + \text{O}_2$  reaction (Figs. 10 and 11), the following general steps for the oxidation of methanol can be proposed:

- i) Chemisorption of methanol on OH sites on the surface of TiO<sub>2</sub> to produce methoxy ( $\text{CH}_3\text{O}_S$ ) species (mono and bidentate coordination) by elimination of water molecules. Part of these methoxy groups are oxidized to formates ( $\text{HCOO}$ ) adsorbed on the titania support, possibly in the metal/support interphase as reported in Au/CeO<sub>2</sub> [15]. In addition, on the catalysts containing Ru, the total dehydrogenation of methanol produces CO linearly adsorbed on Ru metallic sites, but not on the monometallic gold.
- ii) After exposure to oxygen at room temperature,  $\text{CH}_3\text{O}_S$  species are further oxidized to  $\text{HCOO}$  species (bidentate and bridged coordination), being the monodentate methoxy coordination more active. Moreover, it is important to note that the bimetallic Ru-Au catalysts can oxidize adsorbed CO on Ru to  $\text{CO}_2$ . This observation suggests the formation of new, more active, sites able to active  $\text{O}_2$  at low temperature.
- iii) Formate species are oxidized to produce  $\text{CO}_2$  and  $\text{H}_2\text{O}$  (bridged formates are more stable). The oxidation of  $\text{HCOO}$  groups is an activated process and that depends on temperature, being active from 40, 80 °C and RT for Au, Ru and bimetallic catalysts, respectively.

The above observations can be summarized in the following possible reaction pathway:

- 1)  $\text{CH}_3\text{OH}(\text{g}) + \text{Ti-OH} \rightarrow \text{CH}_3\text{O}-\text{Ti} + \text{H}_2\text{O}$
- 2)  $\text{CH}_3\text{O}-\text{Ti} + \text{O}_S \rightarrow \text{HCOO}-\text{Ti} + \text{H}_2\text{O} + \text{V}_O$
- 3)  $\text{HCOO}-\text{Ti} + \text{Au/Ru} \rightarrow \text{Au/Ru}-\text{CO} + \text{Ti-OH}$
- 4)  $\text{Au}-\text{CO} + \text{O}_2/(\text{Au/Ru})-\text{O} \rightarrow \text{CO}_2(\text{g}) + \text{O}_3^{\text{•}}$
- 5)  $\text{O}_2/(\text{Au/Ru})-\text{O} + \text{V}_O \rightarrow \text{Au/Ru} + \text{O}_S$

Where: Ti: site support;  $\text{V}_O$ : surface oxygen vacancy.

This mechanism is in agreement with the proposal by Rousseau et al. [15] for the oxidation of methanol on Au/CeO<sub>2</sub>, where the decomposition of formates in CO and OH species takes place on the periphery of the Au particles and the support, whereas Au oxidizes the adsorbed CO to produce  $\text{CO}_2$ . According to the FTIR spectra in the present work, the absence of the  $\text{CO}-\text{Au}^0$  band (Fig. 11a-d) suggests that formates are completely oxidized to  $\text{CO}_2$ . However, we do not discard the possibility that they were decomposed to CO on the Au particle, as Rousseau et al. have proposed.

Finally, comparing the results of the catalytic activity in the bimetallic Ru-Au 1-1 and the Ru-Au 0.75-1 catalysts (Fig. 1), it can be observed that the first catalyst exhibited higher methanol conversion at RT which was decreased with the increase in the reaction temperature. TEM images show that in bimetallic catalysts gold and ruthenium are in interaction in the particles. Based on this fact, a greater number of bimetallic particles was expected on the Ru-Au 1-1 catalyst due to the higher concentration of Ru in the catalyst, causing a decrease in the active sites for oxygen activation at the interface of Au and TiO<sub>2</sub>.

## 5. Conclusions

Catalytic tests showed that bimetallic Ru-Au/TiO<sub>2</sub> catalysts showed better catalytic performance during the oxidation of methanol, compared to their monometallic counterparts. The optimum atomic Ru: Au ratio was 0.75:1 and had a synergistic effect on the low temperature region. The improvement in the catalytic activity of the bimetallic catalysts can be explained by the interaction of Ru and Au, as confirmed by different characterization techniques. HAADF-STEM and STEM-EDS show the presence of bimetallic structures composed of both Ru and Au metals, and monometallic Ru particles. Moreover, an easier reduction of Au in the bimetallic catalysts was observed by TPR and UV-vis spectroscopy. XPS results showed a shift to higher values in the BE related to Au in the Ru-Au 0.75-1 catalyst, indicating the presence of gold oxidized species as result of the interaction between both metals. Also, DRIFT-CO spectra showed that the interaction between Ru and Au decreased the number of adsorption sites on the surface; they also indicated a change in the nature of gold sites due to the decrease and shift of the  $\text{Au}^0$ -CO band. The FTIR spectra showed that formates, which are the result of the oxidation of methoxy species, are the principal intermediates in the oxidation of methanol. They are produced at lower temperatures and are easily oxidized on the bimetallic catalysts.

## Acknowledgements

We thank DGAPA-UNAM and CONACYT for funding this work within the framework of projects IN105416 and PDNPN1216, respectively and to CONACYT-CONICET 207090 project for funding Mexico-Argentina collaboration. Lina A. Calzada gratefully acknowledges CONACYT for her PhD Scholarship.

## References

- [1] W.B. Li, J.X. Wang, H. Gong, *Catal. Today* 148 (2009) 81–87.
- [2] L.F. Liotta, *Appl. Catal. B* 100 (2010) 403–412.
- [3] G.C. Bond, C. Louis, D.T. Thompson, *Catalysis by Gold*, vol. 6, First ed., Imperial College Press, London, 2006.
- [4] M. Haruta, T. Kobayashi, H. Sano, N. Yamada, *Chem. Lett.* 2 (1987) 405–408.
- [5] J. Gong, C.B. Mullins, *Acc. Chem. Res.* 42 (2009) 1063–1073.
- [6] B. Roldan-Cuenya, *Thin Solid Films* 518 (2010) 3127–3150.
- [7] L. Delannoy, K. Fajerwerg, P. Lakshmanan, C. Potvin, C. Methivier, C. Louis, *Appl. Catal. B* 94 (2010) 117–124.
- [8] D. Andreeva, R. Nedialkova, L. Ilieva, M.V. Abrashev, *Appl. Catal. A* 246 (2003) 29–38.
- [9] M.A. Centeno, M. Paulis, M. Montes, J.A. Odriozola, *Appl. Catal. A* 234 (2002) 65–78.
- [10] V.P. Santos, S.A.C. Carabineiro, P.B. Tavares, M.F.R. Pereira, J.J.M. Órfão, J.J.L. Figueiredo, *Appl. Catal. B* 99 (2010) 198–205.
- [11] S. Scirè, P.M. Riccobene, C. Crisafulli, *Appl. Catal. B* 101 (2010) 109–117.
- [12] S. Minicò, S. Scirè, C. Crisafulli, R. Maggiore, S. Galvagno, *Appl. Catal. B* 28 (2000) 245–251.
- [13] M. Haruta, A. Ueda, S. Tsubota, R.M. Torres Sanchez, *Catal. Today* 29 (1996) 443–447.
- [14] S. Scirè, S. Minicò, C. Crisafulli, C. Satriano, A. Pistone, *Appl. Catal. B* 40 (2003) 43–49.
- [15] S. Rousseau, O. Marie, P. Bazin, M. Daturi, S. Verdier, V. Harlé, *J. Am. Chem. Soc.* 132 (2010) 10832–10841.
- [16] I. Sobczak, N. Kierontczyk, M. Trejda, M. Ziolek, *Catal. Today* 139 (2008) 188–195.

[17] K. Kähler, M.C. Holz, M. Rohe, A.C. Van Veen, M. Muhler, *J. Catal.* 299 (2013) 162–170.

[18] A. Nuhu, J. Soares, M. Gonzalez-Herrera, A. Watts, G. Hussein, M. Bowker, *Top. Catal.* 44 (2007) 293–297.

[19] F. Bocuzzi, A. Chiorino, M. Manzoli, *J. Power Sources* 118 (2003) 304–310.

[20] M. Manzoli, A. Chiorino, F. Bocuzzi, *Appl. Catal. B* 57 (2004) 201–209.

[21] V. Dal Santo, A. Gallo, A. Naldoni, M. Guidotti, R. Psaro, *Catal. Today* 197 (2012) 190–205.

[22] A.K. Datye, J. Shwank, *J. Catal.* 93 (1985) 256–269.

[23] L. Prati, F. Porta, D. Wang, A. Villa, *Catal. Sci. Technol.* 1 (2011) 1624–1629.

[24] F.W. Chang, L.S. Roselin, T.C. Ou, *Appl. Catal. A* 334 (2008) 147–155.

[25] T. Sreethawong, D. Sukjit, P. Ouraipryyan, J.W. Schwank, S. Chavadej, *Catal. Lett.* 138 (2010) 160–170.

[26] O.A. Kirichenko, E.A. Redina, N.A. Davshan, I.V. Mishin, G.I. Kapustin, T.R. Brueva, L.M. Kustov, W. Li, Ch. H. Kim, *Appl. Catal. B* 134–135 (2013) 123–129.

[27] R. Zanella, S. Giorgio, C.R. Henry, C. Louis, *J. Phys. Chem. B* 106 (2002) 7634–7642.

[28] R. Zanella, L. Delannoy, C. Louis, *Appl. Catal. A* 291 (2005) 62–72.

[29] R. Zanella, C. Louis, *Catal. Today* 107–108 (2005) 768–777.

[30] G. Cliff, G.W. Lorimer, *J. Microsc.* 103 (1974) 203–207.

[31] A. Sandoval, A. Aguilar, C. Louis, A. Traverse, R. Zanella, *J. Catal.* 281 (2011) 40–49.

[32] V. Idakiev, L. Ilieva, D. Andreeva, J.L. Blin, L. Gigot, B.L. Su, *Appl. Catal. A* 243 (2003) 25–39.

[33] A. Sandoval, C. Louis, R. Zanella, *Appl. Catal. B* 140–141 (2013) 363–377.

[34] H.G. Manyar, D. Weber, H. Daly, J.M. Thompson, D.W. Rooney, L.F. Gladden, E.H. Stitt, J.J. Delgado, S. Bernal, C. Hardacre, *J. Catal.* 265 (2009) 80–88.

[35] S. Chen, J. Li, Y. Zhang, Y. Zhao, K. Liew, J. Hong, *Catal. Sci. Technol.* 4 (2014) 1005–1011.

[36] P. Reyes, M.E. König, G. Pecchi, I. Concha, M.L. Granados, J.L.G. Fierro, *Catal. Lett.* 46 (1997) 71–75.

[37] A. Pintar, J. Batista, T. Tisler, *Appl. Catal. B* 84 (2008) 30–41.

[38] P.G.J. Koopman, A.P.G. Kieboom, H. Van Bekkum, *J. Catal.* 69 (1981) 172–179.

[39] J.A. Reyes-Esqueda, A. Bautista-Salvador, R. Zanella, *J. Nanosci. Nanotechnol.* 8 (2008) 3843–3850.

[40] O.G. Morales-Saavedra, R. Zanella, *Mater. Chem. Phys.* 124 (2010) 816–830.

[41] S.K. Tyrlık, K. Kurzak, S.L. Randzio, *Transition Met. Chem.* 20 (1995) 330–337.

[42] W. Chen, D. Ghosh, J. Sun, M.C. Tong, F. Deng, S. Chen, *Electrochim. Acta* 53 (2007) 1150–1156.

[43] S. Caliskan, M. Zahmakiran, F. Durap, S. Özkar, *Dalton Trans.* 41 (2012) 4976–4984.

[44] P.S.S. Kumar, A. Manivel, S. Anandan, M. Zhou, F. Grieser, M. Ashokkumar, *Colloids Surf. A* 356 (2010) 140–144.

[45] Y. Lee, D. Kim, S. Shin, S. Oh, *Mater. Chem. Phys.* 100 (2006) 85–91.

[46] J. Sun, S. Fujita, F. Zhao, M. Hasegawa, M. Arai, *J. Catal.* 230 (2005) 398.

[47] A.C. Gluhoi, X. Tang, P. Marginean, B.E. Nieuwenhuys, *Top. Catal.* 39 (2006) 1.

[48] E. Del Río, G. Blanco, S. Collins, M.L. Haro, X. Chen, J.J. Delgado, J.J. Calvino, S. Bernal, *Top. Catal.* 54 (2011) 931–940.

[49] N. Kruse, S. Chenakin, *Appl. Catal. A Gen.* 391 (2011) 367–376.

[50] J. Radnik, C. Mohr, P. Claus, *Phys. Chem. Chem. Phys.* 5 (2003) 172–177.

[51] Y. Kitsudo, A. Iwamoto, H. Matsumoto, K. Mitsuhasha, T. Nishimura, M. Takizawa, T. Akita, Y. Maeda, Y. Kido, *Surf. Sci.* 603 (2009) 2108.

[52] C.L. Bianchi, V. Ragaini, M.G. Cattania, *Mat. Chem. Phys.* 29 (1991) 297–306.

[53] L.E. Chinchilla, C.M. Olmos, A. Villa, A. Carlsson, L. Prati, X. Chen, G. Blanco, J.J. Calvino, A.B. Hungria, *Catal. Today* 253 (2015) 178–189.

[54] S.J. Pennycook, *Ultramicroscopy* 30 (1989) 58–69.

[55] V. Ortalan, A. Uzun, B.C. Gates, N.D. Browning, *Nat. Nanotechnol.* 5 (2010) 843–847.

[56] M. Mihaylov, H. Knözinger, K. Hadjiivanov, B.C. Gates, *Ind. Eng. Chem.* 79 (2007) 795.

[57] K. Chakarova, M. Mihaylov, S. Ivanova, M.A. Centeno, K. Hadjiivanov, *J. Phys. Chem. C* 115 (2011) 21273–21282.

[58] E. Del Río, S.E. Collins, A. Aguirre, X. Chen, J.J. Delgado, J.J. Calvino, S. Bernal, *J. Catal.* 316 (2014) 210–218.

[59] S.E. Collins, J.M. Cies, E. Del Río, J.M. Pintado, S. Trasobares, J.J. Calvino, S. Bernal, *J. Phys. Chem. C* 111 (2007) 14371–14379.

[60] F. Bocuzzi, A. Chiorino, M. Manzoli, D. Andreeva, T. Tabakova, *J. Catal.* 188 (1999) 76–185.

[61] F. Bocuzzi, A. Chiorino, M. Manzoli, *Surf. Sci.* 454–456 (2000) 942–946.

[62] E. Roze, P. Gravejt, E. Quinet, J.L. Rousset, D. Bianchi, *J. Phys. Chem. C* 113 (2009) 1037–1045.

[63] S.Y. Chin, C.T. Williams, M.D. Amiridis, *J. Phys. Chem. B* 110 (2006) 871–882.

[64] K. Hadjiivanov, J.C. Lavalle, J. Lamotte, F. Maugé, J. Saint-Just, M. Che, *J. Catal.* 176 (1998) 415–425.

[65] G.H. Yokomizo, C. Louis, T. Bell, *J. Catal.* 120 (1989) 1–14.

[66] P. Panagiotopoulou, D.I. Kondarides, X.E. Verykios, *J. Phys. Chem. C* 115 (2011) 1220–1230.

[67] M. Nawdali, D. Bianchi, *Appl. Catal. A* 231 (2002) 45–54.

[68] G. Busca, A.S. Elmi, P. Forzatti, *J. Phys. Chem.* 91 (1987) 5263–5269.

[69] S.E. Collins, M.A. Baltanás, A.L. Bonivardi, *Appl. Catal. A* 295 (2005) 126–133.

[70] M.V. Bosco, M.A. Bañares, M.V. Martínez-Huerta, A.L. Bonivardi, S.E. Collins, *J. Mol. Catal. A* 408 (2015) 75–84.

[71] W.-C. Wu, C.-C. Chuang, J.-L. Lin, *J. Phys. Chem. B* 104 (2000) 8719–8724.

[72] D.A. Panayotov, P.A. DeSario, J.J. Pietron, T.H. Brintlinger, L.C. Szymczak, D.R. Rolison, J.R. Morris, *J. Phys. Chem. C* 117 (2013) 15035–15049.

[73] S.E. Collins, L.E. Briand, L.A. Gambaro, M.A. Baltanás, A.L. Bonivardi, *J. Phys. Chem. C* 112 (2008) 14988–15000.

[74] R.B. Barros, A.R. Garcia, L.M. Ilharco, *J. Phys. Chem. B* 105 (2001) 11186–11193.

[75] P. Gazzdicki, P. Jakob, *J. Phys. Chem. C* 114 (2010) 2655–2663.

[76] I. Palacio, O. Rodríguez de la Fuente, *Surf. Sci.* 606 (2012) 1152–1159.

[77] P. Franke, D. Neuschutz, *Binary Systems Part 1, Elements and Binary Systems from Ag-Al to Au-Tl*, vol. 19B1, Springer, Berlin Heidelberg, Germany, 2002, pp. 290–292.

[78] M. Kuhn, J.A. Rodriguez, J. Hrbek, A. Bzowski, T.K. Sham, *Surf. Sci.* 341 (1995) L1011–L1018.